P H Y S I C A L   R E V I E W   L E T T E R S

Angular Dependence of Betatron X-Ray Spectra from a Laser-Wakefield Accelerator

F. Albert,[1,*] B. B. Pollock,[1] J. L. Shaw,[2] K. A. Marsh,[2] J. E. Ralph,[1] Y.-H. Chen,[1] D. Alessi,[1] A. Pak,[1] C. E. Clayton,[2] S. H. Glenzer,[3] and C. Joshi[2]

[1]*Lawrence Livermore National Laboratory, NIF and Photon Sciences, 7000 East Avenue, Livermore California 94550, USA*
[2]*Department of Electrical Engineering, University of California, Los Angeles California 90095, USA*
[3]*SLAC National Accelerator Laboratory, Stanford California 94309, USA*

We present the first measurements of the angular dependence of the betatron x-ray spectrum produced by electrons inside the cavity of a laser-wakefield accelerator. Electrons accelerated up to 300 MeV energies produce a beam of broadband, forward-directed betatron x-ray radiation extending up to 80 keV. The angular resolved spectrum from an image plate-based spectrometer with differential filtering provides data in a single laser shot. The simultaneous spectral and spatial x-ray analysis allows for a three-dimensional reconstruction of electron trajectories with micrometer resolution, and we find that the angular dependence of the x-ray spectrum is showing strong evidence of anisotropic electron trajectories.

The development of efficient x-ray probes with energies larger than 10 kiloelectronvolts (keV) has become essential for high-energy density (HED) science experiments. These experiments produce highly transient matter under extreme states of temperatures and pressures. For instance, high-energy x rays are used to radiograph the dynamics of imploding capsules at the National Ignition Facility [1], or the temperature and pressure of warm dense matter via absorption spectroscopy [2] or scattering [3,4] techniques. Betatron x-ray radiation, produced when relativistic electrons oscillate in a beam-driven [5] or laser-driven [6–8] plasma channel, is an x-ray source holding great promise for future HED experiments. X rays produced in this manner are ultrashort, directional, spatially coherent, and broadband, making them highly attractive as a probe.

Betatron x-ray radiation is readily produced when electrons are accelerated at an ultrahigh gradient in a laser-wakefield accelerator (LWFA) [9–13]. In the three-dimensional (3D), highly nonlinear LWFA regime, when a short but highly intense laser pulse with an intensity $I > 10^{18}$ W/cm^2 is focused inside a plasma, the laser ponderomotive force completely expels the plasma electrons away from the strong intensity regions to form an ion bubble in the wake of the pulse [14]. Electrons trapped at the back of this structure are accelerated and wiggled by the focusing force of the more massive and thus immobile ions to produce broadband, synchrotronlike radiation in the keV energy range [15,16]. Previous work has implied that the betatron x rays have a source size of a few microns [8,17], a divergence of less than 100 mrad [18], and a pulse duration of less than 100 fs [19]. Because betatron x rays are directly related to the electrons emitting them, the radiative properties of the source are also an excellent diagnostic of the acceleration process in a LWFA. The electron beam emittance and size can be inferred from the x-ray beam profile [18,20], spectrum [21,22], or source size [23], using various x-ray spectroscopy

and imaging techniques. In these experiments, however, typical betatron x-ray spectral diagnostics such as filters, crystal spectrometers, single-shot counting mode CCDs, or other semiconductors do not provide single-shot simultaneous spectral and spatial resolution of the radiation.

We present in this Letter the first measurements of the angular dependence of the betatron x-ray spectrum, and show that they can only be explained by assuming an anisotropic electron energy distribution. The highest-energy electrons oscillate about the ion column (the wake axis) predominantly along the direction of the laser polarization vector, whereas lower-energy electrons oscillate more isotropically. A tomographic reconstruction of electron trajectories sheds light on the dynamics of the electrons as they gain energy in the wakefield. These measurements, performed by means of a stacked image-plate spectrometer with differential filtering, have enabled us to observe betatron x rays with energies extending up to 80 keV.

In a LWFA, the motion of an electron accelerated along $\vec{u}_z$ with momentum $\vec{p}$ and position $\vec{r}$ in the wake of a laser pulse can be described by the Lorentz equation of motion, with forces $\vec{F}_\perp$ for the electron transverse oscillations [24] and $\vec{F}_\parallel$ for acceleration,

$$\frac{d\vec{p}}{dt} = \vec{F}_\perp + \vec{F}_\parallel = -m\omega_p^2 \frac{\vec{r}}{2} + \alpha \frac{mc\omega_p}{e}\vec{u}_z, \qquad (1)$$

where m is the electron rest mass, e is the elementary charge, $\omega_p = k_p c = \sqrt{n_e e^2 / m\epsilon_0}$ is the plasma frequency, and k_p is the plasma wave number. Here, n_e is the electron density, ϵ_0 is the vacuum permittivity, and c is the vacuum speed of light. In the blowout three-dimensional nonlinear regime of laser-wakefield acceleration [14], $\alpha = \frac{1}{2}\sqrt{a_0}$ is the normalized accelerating field, where $a_0 = 8.5 \times 10^{-10}\lambda_0$ [μm]$I_L^{1/2}$ [W/cm^2] is the laser normalized vector

potential. The electron trajectory is used to calculate the intensity I radiated by the particle per unit frequency ω and solid angle Ω [25],

$$\frac{d^2I}{d\Omega d\omega} = \frac{e^2\omega^2}{4\pi c}\left|\int_{-\infty}^{\infty}\vec{n}\times(\vec{n}\times\vec{\beta})e^{i\omega(t-(\vec{n}.\vec{r}/c))}dt\right|^2, \quad (2)$$

where $\vec{n}$ is the vector corresponding to the direction of observation and $\beta = v/c$ the normalized electron velocity. For large amplitude oscillations, the wiggler parameter $a_\beta = \gamma k_\beta r_\beta$ is larger than unity, where γ is the electron relativistic factor, r_β the oscillation radius, and $k_\beta = k_p/(2\gamma)^{1/2}$. The spectrum emitted by an electron, observed at an angle θ from the plane of the particle oscillations, can then be approximated by the asymptotic limit [26],

$$\frac{d^2I}{d\Omega d\omega} \propto \frac{\gamma^2\xi^2}{1+\gamma^2\theta^2}\left[K_{2/3}^2(\xi) + \frac{\gamma^2\theta^2}{1+\gamma^2\theta^2}K_{1/3}^2(\xi)\right], \quad (3)$$

where $K_{2/3}$ and $K_{1/3}$ are modified Bessel functions. Here, $\xi = (\omega/\omega_c)(1+\gamma^2\theta^2)^{3/2}$, where the critical frequency $\omega_c \simeq 3a_\beta\gamma^2\omega_\beta$ and $\omega_\beta = \omega_p/(2\gamma)^{1/2}$ is the betatron frequency. For $\theta = 0$, the function $\xi^2 K_{2/3}^2(\xi)$ peaks at $\xi \sim 1/2$ ($\omega \sim 0.5\omega_c$) [26]. The energy corresponding to the maximum intensity of the spectrum (peak energy) will be lower for $\theta > 0$.

The experiment was conducted at the Jupiter Laser Facility, Lawrence Livermore National Laboratory, using the Callisto laser system. Callisto is a 200 TW laser delivering pulses of 60 fs (full width at half maximum [FWHM]) duration with energies up to 12 J at a repetition rate of 1 shot/30 min. The experimental setup is shown in Fig. 1. Using an $f/8$ off-axis parabola, the linearly p polarized laser is focused onto the edge of a 10-mm-long gas cell, with a 500 μm and 1 mm entrance and exit pinhole, respectively. The focal spot, measured at low laser power, is 12 μm (FWHM), and $a_0 \sim 2$. The background electron density of the plasma is measured with interferometry by using a 100 fs probe pulse synchronized with the main laser pulse. The density of the plasma is reconstructed by Abel inverting the measured phase shift imparted by the plasma to the probe beam [27]. As shown in Fig. 1, the electrons are vertically deflected by a 0.42 Tesla, 21.5-cm-long permanent dipole magnet onto two image plates (model FUJI-MS-2040), IP_a and IP_b (a two-screen electron spectrometer [28–30]), used to calculate the energy and deflection of the electron beam. The betatron x rays propagate outside of the vacuum target chamber through a 65 μm mylar window and a 50 μm Al filter to block any residual laser light. The betatron beam profile is measured on IP_a. We use the image plate spectral response function calibrated in [31], and for our experimental configuration, it peaks between 15–20 keV. After transmission through IP_a, the x-ray beam propagates through a series of image plates alternatively stacked
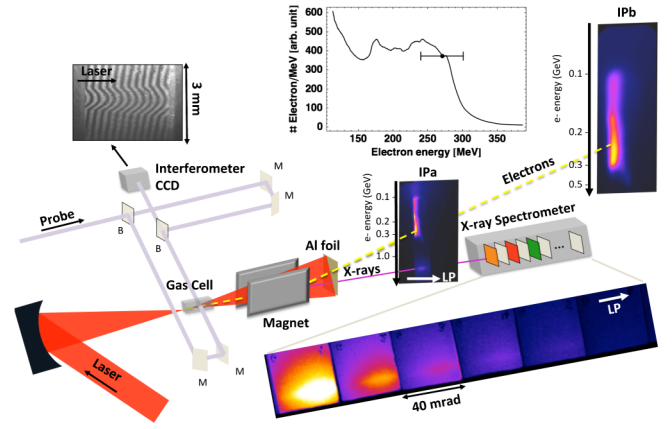

FIG. 1 (color online). Schematic of the experimental setup, showing the $f/8$ off-axis parabola focusing the laser pulse on the gas cell target and the transverse interferometry probe. The interferometer has two beam splitters (B) and four mirrors (M). An example of an interferogram is shown above the interferometer CCD camera. The electrons (dashed line) are dispersed in energy by the magnet centered on the laser axis and located 3.5 cm from the source inside the target chamber and then recorded on image plates (IP_a and IP_b, located 37.2 cm and 111.1 cm away from the magnet exit, respectively). The corresponding retrieved electron beam spectrum is shown on top. Dot with error bar indicates maximum energy of 268 ± 25 MeV. After exiting the vacuum chamber, x rays (solid line) propagate through 7.3 cm of air and through IP_a onto the 15-channel x-ray spectrometer, below which are shown raw images (25 μm pixels) from channels 1–6. LP indicates the laser polarization direction on image plates.

with filters of increasing Z number, located 62.2 cm away from the source, the origin of coordinates. This diagnostic can detect and spectrally resolve broadband x-ray radiation up to 1 MeV through 15 successive channels with an acceptance angle of 40 mrad; we are using its recent characteristics and calibration data [32] for our analysis. Figure 1 shows both the raw x-ray spectrometer data in channels 1–6 and the measured electron beam spectrum (with maximum electron energy 268 ± 25 MeV) for the same shot. Corresponding parameters are laser energy $E = 5.3$ J, $a_0 = 2.33$, and a gas cell filled with 100% He at $n_e = 6 \times 10^{18}$ cm^{-3}. Due to the highly nonlinear nature of the blowout regime and its sensitivity to nonideal laser beam and plasma density profiles, the electron beam spectrum is not monoenergetic as expected from the theory [14].

The first step in our analysis is to retrieve the electron oscillation amplitude in the plasma. This is done using the x-ray spectral data. Figure 2 shows the average on-axis x-ray dose, deposited in each x-ray spectrometer channel, within a spot centered on the beam profile and subtending a solid angle of $\sim 1.1 \times 10^{-6}$ sr from the source. We have fitted the data (dots) with three different theoretical spectra, shown in inset of Fig. 2. This calculated signal takes into account the filters of our setup (Al, mylar, air, first image
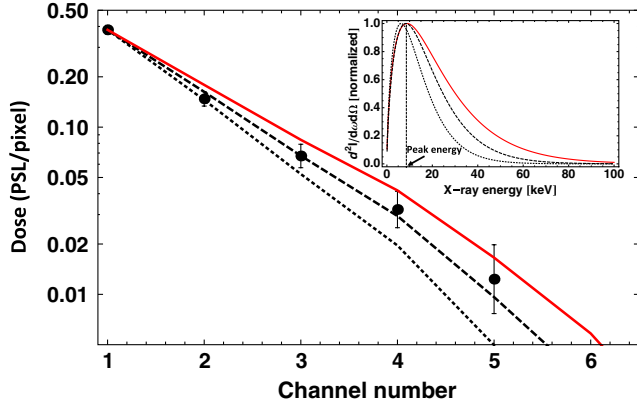
FIG. 2 (color online). X-ray spectrometer signal (dots with error bars), in channels 1–6 (photostimulated luminescence [PSL] per pixel). Calculated dose (normalized to the first data point) for betatron spectra with critical energies of 15 and 20 keV (dotted and dashed lines, respectively) and radiation produced by an electron injected 5 μm off-axis and accelerated up to 268 MeV (red solid line). The inset shows the inferred normalized energy distribution spectrum for each case. Peak energy is shown for the spectrum with $\hbar\omega_c = 20$ keV.

FIG. 3 (color online). (a) Measured and simulated betatron x-ray beam profiles, recorded on IP_a, scanned with a 200 μm pixel size. LP indicates the laser polarization direction. The number of electrons around the propagation axis (positive z direction) is shown in (b) for four distinct groups of electrons accelerated up to $\gamma = 100$, 200, 440, and 520 (dashed, dotted, solid, and dot-dashed lines, respectively). $\theta = 0$ is along the x (vertical) axis and the laser is polarized along $\theta = \pi/2$ rad (y horizontal axis). (c) Sample three-dimensional trajectories are shown for the four groups of electrons in the plasma.

plate) and the response function of each detector channel. In the plasma, the electron oscillation radius damps as it is accelerated up to its final energy, and the spectrum critical energy is not constant throughout the trajectory. A detailed analysis (red solid curve) takes this into account and the spectrum (inset) is calculated numerically as follows. First, the trajectory is calculated by solving Eq. (1) with a fourth-order Runge-Kutta algorithm. All parameters and initial conditions needed to solve Eq. (1), except for the initial oscillation radius r_0, are determined by the experimental conditions. The electron density is $n_e = 6 \times 10^{18}$ cm^{-3}, $\alpha = 0.763$, the electron final energy is 268 MeV ($\gamma \simeq 520$), and the electron initial energy is $\gamma_\Phi = \omega_0/\sqrt{3}\omega_p = 9.85$ [14], which is the Lorentz factor corresponding to the phase velocity of the plasma wave. In our simulation, we use 1500 time steps (with each step $dt = 0.4/\omega_p$) for the whole trajectory. At each time step, the corresponding on-axis ($\theta = 0$) spectrum is calculated with Eq. (2) and accumulated over the whole trajectory. We adjust the initial radius to $r_0 = 5$ μm so that it fits the upper part of the error bars in our data. An upper bound $r_0 = 5$ μm is consistent with previous measurements [17,18,23]. The other spectra shown in inset are calculated using the function $(\omega/\omega_c)^2 K_{2/3}^2(\omega/\omega_c)$ (Eq. (3) for $\theta = 0$ and fixed arbitrary γ) with parameters $\hbar\omega_c = 15$ keV and $\hbar\omega_c = 20$ keV. This is equivalent to a spectrum produced by a single electron oscillating with a constant amplitude and energy (no acceleration). This simple model estimates the on-axis spectrum critical energy $\hbar\omega_c \sim 15$–20 keV (peak energy of 7.5–10 keV).

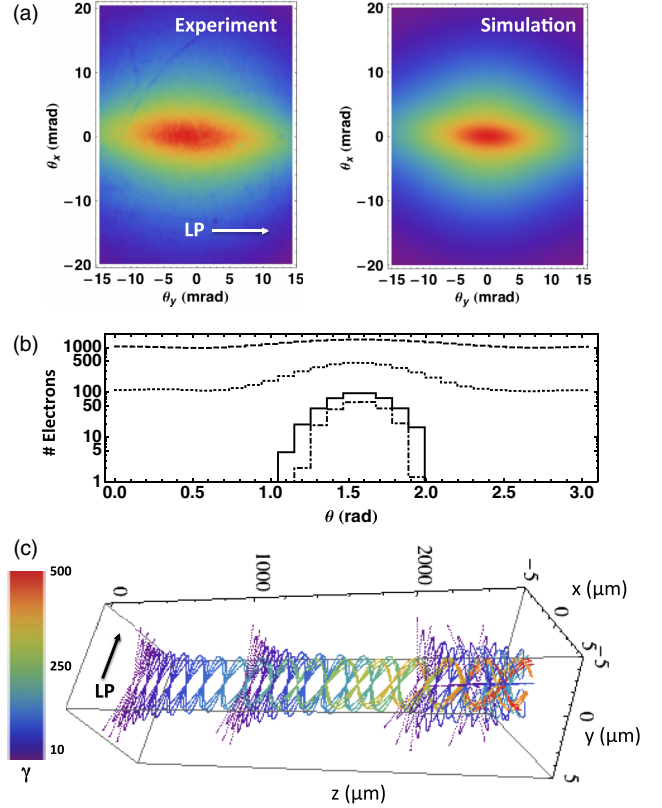The second step is to retrieve the spatial orientation of the electron trajectories. Equation (2) is used to self-consistently match the observed spatial and spectral profiles. The experimental (recorded on IP_a) and simulated beam profiles are shown in Fig. 3(a). Their shape is not completely elliptical as one would expect from a single electron oscillating about the axis [18]. To reproduce the experimental profile using a single particle trajectory tracking method, we use Eq. (2) to map the full spatial and spectral distribution of the betatron radiation. Using a least-squares fitting method, the orientation of electron trajectories for four groups of electrons is adjusted until the simulated beam profile matches the experiment. For the simulation, the particles are distributed on a circle of radius $r_0 = 5$ μm in the transverse (x, y) plane with angular steps of $\pi/30$. Here $\theta = 0$ is along the x axis, the laser is polarized along y ($\theta = \pi/2$). In Fig. 3(b), we show this number of electrons as a function of θ, and for four groups of electrons with different final energies representative of the overall measured spectrum displayed in Fig. 1 (with extrapolation for the lower electron energies). This range

of energies is due to the fact that the electron spectrum is not monoenergetic and that electrons were injected into the wake at different times. The resulting three-dimensional reconstruction of electron trajectories in the plasma is shown in Fig. 3(c) for the same four groups of electrons. For each trajectory, the dephasing length is $L_{dp} = 0.29$ cm, and electrons injected later into the wake end with a lower final energy. This reconstruction is specific to our model, in which we assume (i) complete blowout, (ii) electrons trapped in only the first bucket of the wake, and (iii) cylindrical symmetry in the radial focusing forces. Several factors can explain the anisotropy observed in the electron distribution in Fig. 3(b). In our case, the high-energy particles oscillate primarily along the laser polarization direction. This is suggestive of these particles gaining energy from the wakefield and interacting with the transverse laser field [33]. The lower-energy particles have a more isotropic distribution around the propagation axis possibly because they are injected into the wake at a later time, when the laser pulse has already undergone substantial longitudinal pulse compression [34]. At $n_e = 6 \times 10^{18}$ cm^{-3} and for a laser power $P = 44$ TW (50% coupling efficiency), the dephasing length L_{dp}[cm] $\simeq (P[TW])^{1/6}(10^{18}$[cm$^{-3}]/n_e)^{4/3} \simeq 0.2^{+0.13}_{-0.04}$ cm is shorter than the length of the gas cell, and the most energetic electrons may interact with the back of the laser pulse to oscillate primarily in the direction of laser polarization. However, other effects, such as pulse front tilt [35], have also been shown to strongly influence the direction of the electron oscillations and subsequent betatron radiation [36].

Finally, we compare the experimental angular dependence of the betatron x-ray spectrum with the angular dependence of the spectrum calculated from the trajectories of Fig. 3(c). Figure 4 shows the variation of the peak x-ray energy with the observation angle, and the latter is defined in the inset. For each observation angle, we measure the dose in channels 1–6 of the detector and fit with the function $(\omega/\omega_c)^2 K^2_{2/3}(\omega/\omega_c)$ following the same method and peak energy definition as in Fig. 2. The error bars reflect the range of peak energies that fit the measured spectrum. We measure similar trends (decrease of peak energy from ~10 keV on axis to lower values at higher observation angles) on shots done with similar laser energies and plasma conditions. The experimental data of Fig. 4 are then fitted with two different theoretical spectra obtained from (i) the synchrotron radiation asymptotic limit [Eq. (3)] where $\hbar\omega_c = 20$ keV is fixed and θ is the observation angle and (ii) the spectrum emitted by the multiple trajectories of Fig. 3(c), calculated from Eq. (2) where the vector $\vec{n}$ is adjusted with the observation angle. As seen in Fig. 4, the simple model does not reproduce the experimental angular dependence of the x-ray spectrum because it assumes that electrons oscillate along only one direction. Although the most energetic particles primarily
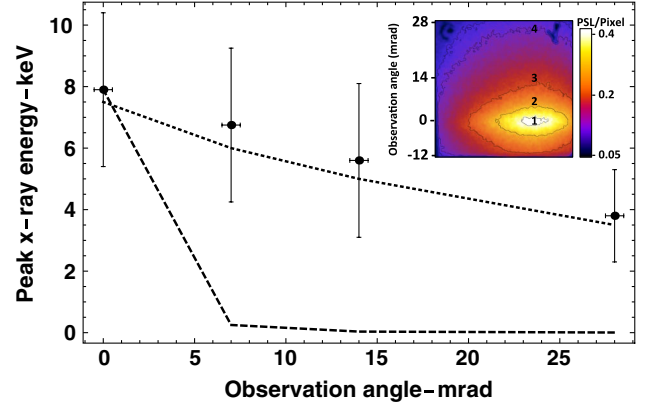

FIG. 4 (color online). Peak experimental betatron x-ray energy as a function of the angle of observation (dots with error bars). The spectrum was measured on axis and at 7, 14, and 28 mrad corresponding to respective vertical positions 1, 2, 3, 4 indicated in the inset showing the beam profile on the first spectrometer channel. The two curves show the theoretical peak energy for Eq. (3) (dashed line) and the full set of electron trajectories (dotted line).

oscillate along the laser polarization axis, a larger number of lower-energy electrons oscillate with a wider range of angles in the transverse plan. This results in a softer decrease of the peak x-ray energy with increasing observation angles.

In conclusion, we have shown that experimental observations of the angular dependence of the betatron spectrum can be explained by taking into account the oscillations of accelerated electrons with an anisotropic electron energy distribution in a LWFA. In the future, this technique can be further improved to take into account the angular spread, injection phase, and spread in the injection radius, thereby making the betatron radiation a powerful single-shot self-probe of the LWFA. Characterizing the angular dependance of the betatron x-ray spectrum is important for near-term single-shot HED experiments using pump-probe, scattering, imaging, and spectroscopic techniques where spatially-resolved spectral mapping of the beam is needed.

*albert6@llnl.gov

[1] D. Hicks *et al.*, Phys. Plasmas **19**, 122702 (2012).

[2] A. Benuzzi-Mounaix, F. Dorchies, V. Recoules, F. Festa, O. Peyrusse, A. Levy, A. Ravasio, T. Hall, M. Koenig, N. Amadou, E. Brambrink, and S. Mazevet, Phys. Rev. Lett. **107**, 165006 (2011).

[3] A. L. Kritcher, P. Neumayer, J. Castor, T. Doppner, R. W. Falcone, O. L. Landen, H. J. Lee, R. W. Lee, E. C. Morse, A. Ng, S. Pollaine, D. Price, and S. H. Glenzer, Science **322**, 69 (2008).

[4] S. H. Glenzer and R. Redmer, Rev. Mod. Phys. **81**, 1625 (2009).

[5] S. Wang, C. E. Clayton, B. E. Blue, E. S. Dodd, K. A. Marsh, W. B. Mori, C. Joshi, S. Lee, P. Muggli, T. Katsouleas, F. J. Decker, M. J. Hogan, R. H. Iverson, P. Raimondi, D. Walz, R. Siemann, and R. Assmann, Phys. Rev. Lett. **88**, 135004 (2002).

[6] A. Rousse, K. Ta Phuoc, R. Shah, A. Pukhov, E. Lefebvre, V. Malka, S. Kiselev, F. Burgy, J.-P. Rousseau, D. Umstadter, and D. Hulin, Phys. Rev. Lett. **93**, 135005 (2004).

[7] S. Corde, K. Ta Phuoc, G. Lambert, R. Fitour, V. Malka, and A. Rousse, Rev. Mod. Phys. **85**, 1 (2013).

[8] S. Kneip *et al.*, Nat. Phys. **6**, 980 (2010).

[9] T. Tajima and J. M. Dawson, Phys. Rev. Lett. **43**, 267 (1979).

[10] S. P. D. Mangles, C. D. Murphy, Z. Najmudin, A. G. R. Thomas, J. L. Collier, A. E. Dangor, E. J. Divall, P. S. Foster, J. G. Gallacher, C. J. Hooker, D. A. Jaroszynski, A. J. Langley, W. B. Mori, P. A. Norreys, F. S. Tsung, R. Viskup, B. R. Walton, and K. Krushelnick, Nature (London) **431**, 535 (2004).

[11] C. G. R. Geddes, C. Toth, J. V. Tilborg, E. Esarey, C. B. Schroeder, D. Bruhwiler, C. Nieter, J. Cary, and W. P. Leemans, Nature (London) **431**, 538 (2004).

[12] J. Faure, Y. Glinec, A. Pukhov, S. Kiselev, S. Gordienko, E. Lefebvre, J.-P. Rousseau, F. Burgy, and V. Malka, Nature (London) **431**, 541 (2004).

[13] X. Wang *et al.*, Nat. Commun. **4**, 1988 (2013).

[14] W. Lu, M. Tzoufras, C. Joshi, F. S. Tsung, W. B. Mori, J. Vieira, R. A. Fonseca, and L. O. Silva, Phys. Rev. ST Accel. Beams **10**, 061301 (2007).

[15] F. Albert, R. Shah, K. Ta Phuoc, R. Fitour, F. Burgy, J.-P. Rousseau, A. Tafzi, D. Douillet, T. Lefrou, and A. Rousse, Phys. Rev. E **77**, 056402 (2008).

[16] S. Fourmaux, S. Corde, K. Ta Phuoc, P. M. Leguay, S. Payeur, P. Lassonde, S. Gnedyuk, G. Lebrun, C. Fourment, V. Malka, S. Sebban, A. Rousse, and J. C. Kieffer, New J. Phys. **13**, 033017 (2011).

[17] R. C. Shah, F. Albert, K. Ta Phuoc, O. Shevchenko, D. Boschetto, A. Pukhov, S. Kiselev, F. Burgy, J.-P. Rousseau, and A. Rousse, Phys. Rev. E **74**, 045401(R) (2006).

[18] K. Ta Phuoc, S. Corde, R. Shah, F. Albert, R. Fitour, J.-P. Rousseau, F. Burgy, B. Mercier, and A. Rousse, Phys. Rev. Lett. **97**, 225002 (2006).

[19] K. Ta Phuoc, R. Fitour, A. Tafzi, T. Garl, N. Artemiev, R. Shah, F. Albert, D. Boschetto, A. Rousse, D.-E. Kim, A. Pukhov, V. Seredov, and I. Kostyukov, Phys. Plasmas **14**, 080701 (2007).

[20] S. Corde, C. Thaury, A. Lifschitz, G. Lambert, K. Ta Phuoc, X. Davoine, R. Lehe, D. Douillet, A. Rousse, and V. Malka, Nat. Commun. **4**, 1501 (2013).

[21] G. R. Plateau, C. G. R. Geddes, D. B. Thorn, M. Chen, C. Benedetti, E. Esarey, A. J. Gonsalves, N. H. Matlis, K. Nakamura, C. B. Schroeder, S. Shiraishi, T. Sokollik, J. Van Tilborg, C. Toth, S. Trotsenko, T. S. Kim, M. Battaglia, T. Stohlker, and W. P. Leemans, Phys. Rev. Lett. **109**, 064802 (2012).

[22] M. Schnell, A. Savert, B. Landgraf, M. Reuter, M. Nicolai, O. Jackel, C. Peth, T. Thiele, O. Jansen, A. Pukhov, O. Willi, M. C. Kaluza, and C. Spielmann, Phys. Rev. Lett. **108**, 075001 (2012).

[23] S. Kneip, C. McGuffey, J. L. Martins, M. S. Bloom, V. Chvykov, F. Dollar, R. Fonseca, S. Jolly, G. Kalintchenko, K. Krushelnick, A. Maksimchuk, S. P. D. Mangles, Z. Najmudin, C. A. J. Palmer, K. Ta Phuoc, W. Schumaker, L. O. Silva, J. Vieira, V. Yanovsky, and A. G. R. Thomas, Phys. Rev. ST Accel. Beams **15**, 021302 (2012).

[24] I. Kostyukov, S. Kiselev, and A. Pukhov, Phys. Plasmas **10**, 4818 (2003).

[25] J. Jackson, *Classical Electrodynamics* (Wiley, New York, 1988).

[26] E. Esarey, B. A. Shadwick, P. Catravas, and W. P. Leemans, Phys. Rev. E **65**, 056505 (2002).

[27] A. E. Pak, Ph.D. thesis, University of California Los Angeles, 2010.

[28] I. Blumenfeld, C. E. Clayton, F.-J. Decker, M. J. Hogan, C. Huang, R. Ischebeck, R. Iverson, C. Joshi, T. Katsouleas, N. Kirby, W. Lu, K. A. Marsh, W. B. Mori, P. Muggli, E. Oz, R. H. Siemann, D. Walz, and M. Zhou, Nature (London) **445**, 741 (2007).

[29] C. E. Clayton, J. E. Ralph, F. Albert, R. A. Fonseca, S. H. Glenzer, C. Joshi, W. Lu, K. A. Marsh, S. F. Martins, W. B. Mori, A. Pak, F. S. Tsung, B. B. Pollock, J. S. Ross, L. O. Silva, and D. H. Froula, Phys. Rev. Lett. **105**, 105003 (2010).

[30] B. B. Pollock, C. E. Clayton, J. E. Ralph, F. Albert, A. Davidson, L. Divol, C. Filip, S. H. Glenzer, K. Herpoldt, W. Lu, K. A. Marsh, J. Meinecke, W. B. Mori, A. Pak, T. C. Rensink, J. S. Ross, J. Shaw, G. R. Tynan, C. Joshi, and D. H. Froula, Phys. Rev. Lett. **107**, 045001 (2011).

[31] B. R. Maddox, H. S. Park, B. A. Remington, N. Izumi, S. Chen, C. Chen, G. Kimminau, Z. Ali, M. J. Haugh, and Q. Ma, Rev. Sci. Instrum. **82**, 023111 (2011).

[32] C. D. Chen, J. A. King, M. H. Key, K. U. Akli, F. N. Beg, H. Chen, R. R. Freeman, A. Link, A. J. Mackinnon, A. G. MacPhee, P. K. Patel, M. Porkolab, R. B. Stephens, and L. D. V. Woerkom, Rev. Sci. Instrum. **79**, 10E305 (2008).

[33] S. P. D. Mangles, A. G. R. Thomas, M. C. Kaluza, O. Lundh, F. Lindau, A. Persson, F. S. Tsung, Z. Najmudin, W. B. Mori, C.-G. Wahlstrom, and K. Krushelnick, Phys. Rev. Lett. **96**, 215001 (2006).

[34] J. Faure, Y. Glinec, J. J. Santos, F. Ewald, J.-P. Rousseau, S. Kiselev, A. Pukhov, T. Hosokai, and V. Malka, Phys. Rev. Lett. **95**, 205003 (2005).

[35] A. Popp, J. Vieira, J. Osterhoff, Z. Major, R. Horlein, M. Fuchs, R. Weingartner, T. P. Rowlands-Rees, M. Marti, R. A. Fonseca, S. F. Martins, L. O. Silva, S. M. Hooker, F. Krausz, F. Gruner, and S. Karsch, Phys. Rev. Lett. **105**, 215001 (2010).

[36] M. Schnell, A. Savert, I. Uschmann, M. Reuter, M. Nicolai, T. Kampfer, B. Landgraf, O. Jackel, O. Jansen, A. Pukhov, M. C. Kaluza, and C. Spielmann, Nat. Commun. **4**, 2421 (2013).